IEEE Journal of Microwaves

Received 22 October 2025; revised 30 November 2025; accepted 30 November 2025.

Digital Object Identifier 10.1109/JMW.2025.3642178

Wireless Power Transfer-Enabled Optogenetic Stimulation of Hypoglossal Motoneurons in Mice for Functional Studies in Obstructive Sleep Apnea

GIACOMO PAOLINI [1] (Member, IEEE), GIULIA BATTISTINI [1] (Member, IEEE), ELISA AUGELLO[1] (Graduate Student Member, IEEE), STEFANO BASTIANINI[2], CHIARA BERTEOTTI[2], DARIO CORACI[2], VIVIANA LO MARTIRE[2], DIEGO MASOTTI [1] (Senior Member, IEEE), ELENA MIGLIORANZA[2], SIMONE TROVARELLO [1] (Member, IEEE), EMILIA VOLINO[2], GIOVANNA ZOCCOLI [2], AND ALESSANDRA COSTANZO [1] (Fellow, IEEE)

[1]DEI "G. Marconi", University of Bologna, 40136 Bologna, Italy
[2]DIBINEM, University of Bologna, 40126 Bologna, Italy

CORRESPONDING AUTHOR: Giacomo Paolini (email: giacomo.paolini4@unibo.it).

This work was supported in part by the European Union (NextGenerationEU) under the Italian National Recovery and Resilience Plan (NRRP) within the framework of PRIN (Project of Relevant National Interest) 2022 NRRP project "ESTROSA: Energy-autonomous System for Treatment of Obstructive Sleep Apnea" (CUP: J53D23014050001) and in part by the European Union under the NextGenerationEU programme (National Recovery and Resilience Plan (NRRP) – Mission 4 Component 2, Investment 1.4 – D.D. 1033 17/06/2022, CN00000023).

ABSTRACT Obstructive sleep apnea (OSA) is a widespread sleep-related breathing disorder linked to cardiovascular and cognitive complications. Although continuous positive airway pressure (CPAP) remains the standard therapy, poor patient adherence limits its effectiveness. Hypoglossal nerve stimulation is a promising alternative, and optogenetic activation offers superior spatiotemporal precision. However, before clinical use, this approach requires thorough validation in animal models using platforms that preserve natural behavior. This work proposes a fully wireless alternative to conventional optogenetic platforms which rely on tethered optical fibers, restricting the animal's mobility, inducing tissue inflammation, and limiting experimental flexibility. Fully implantable, miniaturized systems with wireless power transfer (WPT) and control capabilities address the need for reduced invasiveness, enabling natural behavior and long-term studies. We present the design and the in vivo validation of a battery-free, wireless optogenetic platform for in vivo studies on small laboratory mice, designed to minimize device size, weight, and invasiveness. A conformal WPT system of inductive resonant transmitting coils at 13.56 MHz is proposed to be integrated into the laboratory cage hosting the mice. A miniaturized, lightweight, and flexible receiving system (weighing less than 0.6 g) is designed to be implanted on the back of the mouse in a saddle-like configuration. The implanted device hosts the rectification circuitry, used to drive a microscale light-emitting diode (LED) positioned over the hypoglossal nuclei. In this way, optogenetic stimulation without fiber-optic tethers is obtained. Full-wave electromagnetic simulations and experimental validation are first carried out to assess the WPT link performance, demonstrating high tolerance to relative translational and angular displacement between the transmitting and receiving coils, and stable harvested power across the cage volume. For a transmitted power of 1.5 W, a minimum DC power of 20 mW has been obtained in the worst-case position of the mouse inside the cage, sufficient for the LED operation. Finally, in vivo experiments are presented, confirming not only the LED activation but also the hypoglossal nerve stimulation, fully compliant with the radiant flux requirements for optogenetic neurostimulation under realistic conditions. These results demonstrate the feasibility and robustness of the proposed WPT system for untethered, battery-free optogenetic stimulation in lightweight murine models with OSA, providing a platform for preclinical neuroscience research, paving the way toward next-generation low-invasiveness neuromodulation strategies.

INDEX TERMS Coils, LED, near-field, optogenetics, OSA, radiofrequency, wireless power transfer.

I. INTRODUCTION

Obstructive sleep apnea (OSA) is a common chronic sleep-related breathing disorder, characterized by recurrent episodes of partial or complete obstruction of the upper airway during sleep, which result in intermittent reductions or cessations of airflow [1], due to an exaggerated reduction of lingual muscle tone during sleep, particularly during rapid eye movement (REM) sleep, which contributes to upper airway collapse [2]. These recurrent obstructive events trigger a cascade of physiological consequences, leading to hemoglobin desaturation, frequent arousals, and fragmentation of sleep architecture, ultimately causing daytime sleepiness and reduced quality of life. Beyond its immediate symptoms, OSA has been associated with severe comorbidities, including cardiovascular disease, hypertension, arrhythmia, stroke, metabolic dysfunction, and neurocognitive impairment [3].

Continuous positive airway pressure (CPAP) is currently the gold standard therapy: a steady stream of pressurized air delivered through a nasal or oronasal mask maintains the airway patency during sleep, effectively preventing airway collapse. However, CPAP is limited by poor adherence, with compliance rates ranging between 40% and 85% due to discomfort, noise, mask leakage, or the perception of invasiveness in their nightly routine [4], underscoring the urgent need for alternative therapeutic solutions.

Hypoglossal nerve stimulation is a clinically validated alternative that improves airway patency by electrically activating the genioglossus (GG) muscle, promoting tongue protrusion, and reducing the likelihood of airway obstruction during sleep [5]. Current clinically approved devices provide promising outcomes but typically require the surgical implantation of a pulse generator connected via leads to stimulating electrodes around the nerve [6]. This approach remains invasive, expensive, and carries risks such as infection, nerve injury, and device-related complications [7]. Recently, implantable devices capable of stimulating the hypoglossal nerve have been approved for human use. However, these devices are applicable only to a few individuals, and they act solely unilaterally or on the anterior part of the tongue [8].

In this context, optogenetic neurostimulation has emerged as a powerful technique to modulate neuronal activity with high spatiotemporal precision. By introducing light-sensitive ion channels, such as channelrhodopsin-2 (ChR2) or halorhodopsin (NpHR), into specific neuronal populations, neurons can be selectively activated or inhibited with optical stimulation. Targeting hypoglossal motoneurons offers a promising strategy to prevent upper airway collapse in OSA, combining functional specificity with reduced invasiveness [9]. However, despite its considerable potential as a therapeutic strategy, its clinical translation still remains unproven and requires thorough validation in animal models. Since its DNA was completely sequenced in 2002, the mouse has become the species of choice in biomedical research, including the field of sleep breathing disorders [10]. The small size of the mouse (typically 20–25 g of weight, with a skull of 2 x 1 cm) has increased its use in research; however, it requires device solutions miniaturized and low-profile to match its anatomical and behavioral characteristics. To enable accurate and physiologically relevant experimentation, wireless optogenetic systems are highly desirable, as they overcome the limitations of tethered fiber optics, reduce stress and behavioral constraints, and allow long-term naturalistic investigations.

Conventional platforms based on tethered fibers or head-mounted LEDs [11] restrict mobility, strain brain tissue, cause inflammation, and suffer from optical attenuation in deep brain regions. These limitations hinder long-term naturalistic behavioral studies, motivating the development of fully wireless, miniaturized devices for precise optogenetic stimulation in freely moving small animals [12].

Early approaches based on wireless battery-powered head-mounted devices eliminated tethers but still added bulk and weight, altering natural behaviors [12], [13]. Thus, more recent advances have focused on battery-free, fully implantable optoelectronic systems powered by wireless power transfer (WPT). These devices typically operate in the high-frequency (HF) radiofrequency (RF) band (3–30 MHz) using inductive coupling or inductive resonant coupling [14], a technology widely implemented in consumer electronics for contactless energy transfer. RF energy is delivered from a transmitting (TX) coil integrated into the experimental cage to a subdermal receiving (RX) coil system implanted in the animal. The harvested energy is rectified into DC and used to drive a microscale light-emitting diode (μ-LED) positioned at the target site. However, current state-of-the-art battery-free wireless optogenetic systems [15], [16], [17], [18] still face key challenges, including limited tolerance to movement-induced relative translational and angular displacement between the TX and RX coils, mechanical strain on the skull, and the risk of biasing natural behaviors.

Therefore, in this work, we aim to overcome these limitations by introducing a flexible, conformal WPT system at 13.56 MHz, specifically designed for battery-free optogenetic stimulation of hypoglossal motoneurons controlling lingual muscle tone, with the aim of preventing upper airway collapse and thus the onset of OSA in small murine models.

Previous works [19], [20], [21] by the authors have already demonstrated the feasibility of near-field WPT for implantable optogenetic systems, together with the relevant electromagnetic (EM) design principles and optimization strategies. Building upon these foundations, the present work further advances the field by providing complete experimental validation and in vivo demonstration of the fully integrated WPT-enabled optogenetic platform. The study includes a comprehensive characterization of the WPT link, with accurate measurements of coupling coefficients, RF-to-RF efficiencies, and end-to-end RF-to-DC performance, and reports the first successful wireless optogenetic stimulation of hypoglossal motoneurons in mice, achieving a clear motor response with only 2.4 mW of radiant power. These results confirm the effectiveness of the developed system and its potential to enable efficient, battery-free optical stimulation in freely moving small animal models.

The system comprises a transmitting series-connected multi-coil array designed to deliver uniform, multi-directional power throughout the cage, and a pair of compact receiving coils implanted on the animal's back in a saddle-like configuration. This placement strategically enhances tolerance to positional relative translational and angular displacement between TX and RX coils, compared to state-of-the-art approaches [15], [16], [17], [18], where receivers are mounted on the skull, a region with increased rotational dynamics than the back, combined with limited surface area that restricts receiver size and power harvesting. By relocating the receiver to the back, our design maximizes the effective harvesting area, reduces mechanical load on the skull, thus preserving the animal's natural mobility. The receiver implant integrates a rectification circuit to power an implanted μ-LED precisely positioned over the hypoglossal nuclei, the motor centers responsible for tongue contractions. This solution ensures uninterrupted light emission independent of the animal's orientation. Most importantly, by leveraging WPT, the system eliminates the need for fiber-optic tethers and other wired connections, enabling naturalistic, untethered behavior during experiments.

II. NEAR-FIELD WPT SYSTEM DESIGN

These considerations highlight the need for a WPT platform that combines miniaturization, efficient and stable energy harvesting, and designed to reduce interference with natural behavior in small murine models. Building on these requirements, in this section, we present and characterize a conformal, soft, and flexible WPT system specifically engineered to enable the battery-free operation of an implanted μ-LED.

The proposed system, initially conceived in [20], is illustrated in Fig. 1, and it relies on an inductive resonant link operating at 13.56 MHz. A conformal TX array of series-connected coils powers a pair of miniaturized RX coils implanted on the mouse's back in a saddle-like configuration. Coverage of the RX coils with a polymeric material could provide protection and biocompatibility, and an alternative approach could avoid subcutaneous implantation entirely by designing the RX as an external conformal fixture. Both strategies could be explored to assess feasibility and tolerability in freely moving animals. On the same RX module, the power rectification circuit is integrated and DC-connected to a μ-LED aligned with the hypoglossal nuclei, where the motoneurons innervating the tongue are located.

This TX coils arrangement [20] has proved to ensure spatially uniform power coverage throughout the quasi-cylindrical experimental cage of 50 mm of height and 50 mm of radius, integrated into a whole-body plethysmograph (Fig. 1(b)), allowing simultaneous recording of the mouse's vital signals during experiments. An aperture is included on the curved wall, ensuring the animal's nourishment throughout the procedure.

Moreover, the strategic saddle-like RX placement not only increases the effective harvesting area but also improves tolerance to real-world relative coil displacement and angular

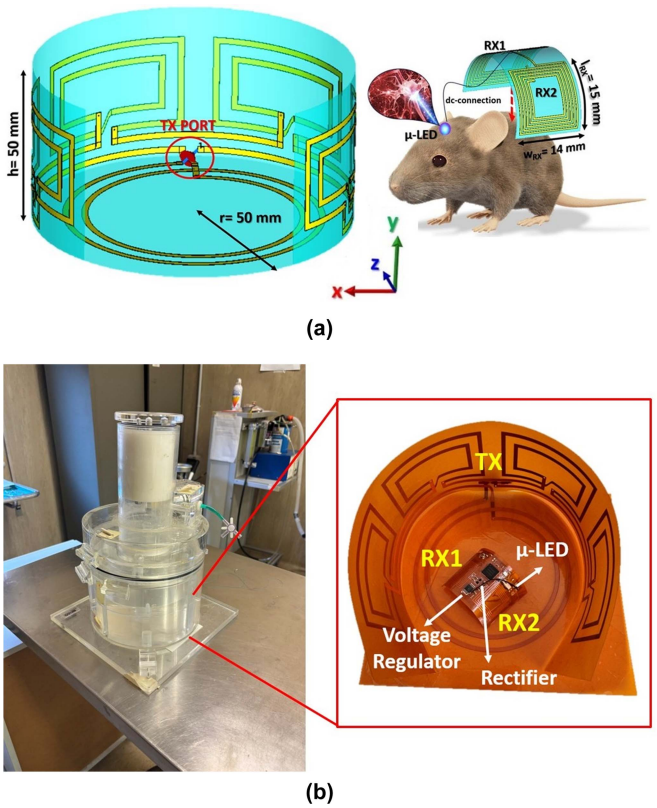

FIGURE 1. (a) Wireless power transfer system schematic overview: transmitting multi-coil array (left) and saddle-like receiving device implantable on the mouse's back (right); (b) photo of the plethysmograph setup with a callout highlighting the fabricated prototype and a detailed view of the receiving system, including two receiving coils, rectifier, voltage regulator, and LED. [19].

orientation, since the degrees of freedom of the back's movements and rotations are more limited compared to those of the head, while also avoiding additional bulk and dimension constraints on the small cranial region. As a result, the system ensures reliable energy transfer and continuous light delivery regardless of the mouse's movements and positions, thereby enhancing operational robustness, animal comfort, and experimental reproducibility.

A. ELECTROMAGNETIC DESIGN OF THE TRANSMITTING MULTI-COIL ARRAY

The TX array, shown on the left side of Fig. 1(a) and detailed in Fig. 2(a), consists of five series-connected coils, four rectangular ones distributed along the lateral wall, and a circular one placed on the cage floor. Their dimensions have been EM-optimized in CST Microwave Studio to ensure continuous magnetic field coverage of the entire region occupied by the mouse, regardless of its position and orientation [20]. The flexible substrate selected for the TX array enables the coils to conform and to adhere along the cylindrical chamber walls, markedly differing from the conventional approach of using a single transmitting coil, which typically cannot provide a uniform field distribution, thus requiring higher transmitted

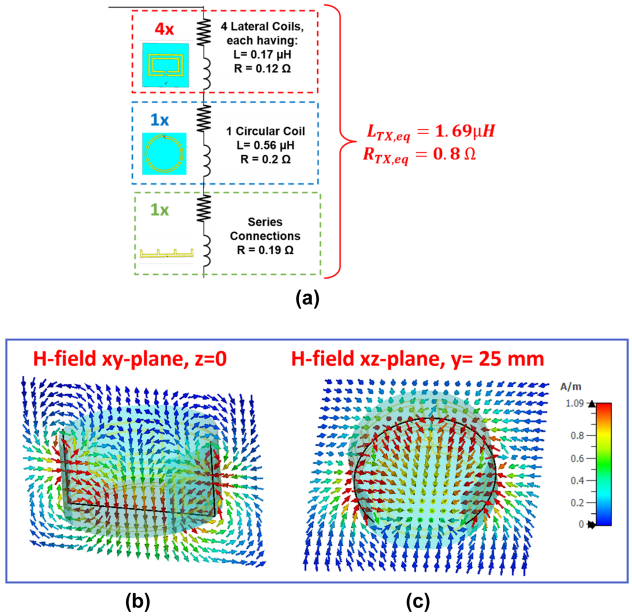

FIGURE 2. **Detailed view of the TX multi-coil array system: (a) Individual coils and connections composing the array, together with their equivalent inductance and loss resistance; simulated magnetic field (H-field) distribution obtained by cutting the semi-cylindrical chamber in half, (b) vertically along the axial (*xy*-plane), and (c) horizontally along the transverse (*xz*-plane) sections.**

power, often 8–10 W in state-of-the-art systems [16], to ensure the receiver always harvests sufficient power regardless of the animal's position. In contrast, our flexible multi-coil design, with series-connected smaller coils, achieves a uniform magnetic field distribution while maintaining effective power transfer within safety limits for implantable applications. As demonstrated in [22], arrays of smaller coils provide a more adaptable and focused magnetic flux distribution, particularly under dynamic WPT conditions, and series connection reduces sensitivity to misalignments between TX and RX, as analytically detailed in [23].

The four identical rectangular coils, with dimensions 52 x 30 mm^2, are positioned along the cylinder walls spaced by 4 mm; the circular one has a 30-mm-radius covering the bottom, as shown in Fig. 1(a). All coils are realized with 35-μm-thick copper traces, 2 mm in width, arranged in two turns, with a spacing of 4 mm. This configuration was engineered to achieve, at the operating frequency of 13.56 MHz, a constructive vectorial combination of the magnetic fields, resulting in uniform and multi-directional 3D power coverage inside the cage. The predicted 3D field distribution is illustrated in Fig. 2 for two representative cross-sectional planes of the cylindrical chamber. Fig. 2(b) shows a vertical axial plane passing through the central axis of the structure (*xy*-plane, $z = 0$, see Fig. 1(a)), which cuts the cylinder into two symmetric halves and allows visualization of the field distribution along the cage height and diameter. Fig. 2(c) shows a horizontal transverse plane intersecting the chamber at $y = 25$ mm, corresponding to the maximum elevation reached by the mouse within the chamber and to the expected location of the implanted RX. In the axial plane, the series connection of the coils produces a constructive superposition of the magnetic field going from the bottom coil to the lateral ones, enhancing coverage in the center of the cage. In the transversal plane, the four lateral coils collectively provide coverage across multiple orientations, ensuring effective power delivery throughout the experimental volume. The resulting total equivalent inductance and loss resistance resulted to be $L_{TX,eq} = 1.69$ μH and $R_{TX,eq} = 0.8$ Ω, respectively, and have been computed from the EM simulations with reference to the circuit model shown in Fig. 2(a).

B. ELECTROMAGNETIC CIRCUITAL CO-DESIGN AND OPTIMIZATION OF THE RECEIVING IMPLANTABLE DEVICE

The implantable RX device, depicted on the right-hand side of Fig. 1(a), comprises two small identical rectangular coils with five turns each, spaced by 0.9 mm with 35-μm-thick and 0.41-mm-wide copper lines in rectangular shape, measuring $w_{RX} = 14$ mm and $l_{RX} = 15$ mm. Its geometry and positioning have been carefully designed and optimized from an EM standpoint to maximize energy harvesting, independent of the mouse's movements or orientation, thereby ensuring continuous operation of the μ-LED. Each RX coil exhibits a simulated inductance of $L_{RX,i=\ 1,2} = 0.43$ μH and a loss resistance of $R_{RX,i=\ 1,2} = 0.38$ Ω [21].

To assess the biological tissue impact on the EM performance, simulations were performed by modeling the receiver encapsulated between two 100-μm polyimide layers and embedded within a 3.5 cm diameter tissue cylinder, represented as the union of four concentric cylindrical layers (skin, 0.29-mm-thick; fat, 2.87-mm-radius; muscle, 7.17-mm-thick; blood, 7.17-mm-thick) with realistic dielectric properties at 13.56 MHz [24].

The simulation results demonstrated that the TX–RX link, in terms of inductive coupling, remains essentially unchanged when the receiver is embedded in biological tissue and moved across different positions and orientations within the cage. These findings indicate that, under the considered scenarios, biological tissues do not significantly influence the inductive coupling between the TX and RX coils and were therefore considered sufficient to reliably represent realistic in vivo operating scenarios.

Although real in vivo experimental conditions can involve additional sources of variability, the system was deliberately designed to operate in the lower HF band at 13.56 MHz, where magnetic near-field coupling is dominant and tissue absorption of the magnetic field is intrinsically limited. Thus, this design choice minimizes biological loading effects and ensures robust operation under realistic experimental conditions.

In addition, a preliminary EM safety assessment was carried out by evaluating the specific absorption rate (SAR) within the multilayer tissue model. Full-wave simulations were performed by applying the maximum transmitted power (1.5 W) used in the in vivo experiments. The obtained SAR

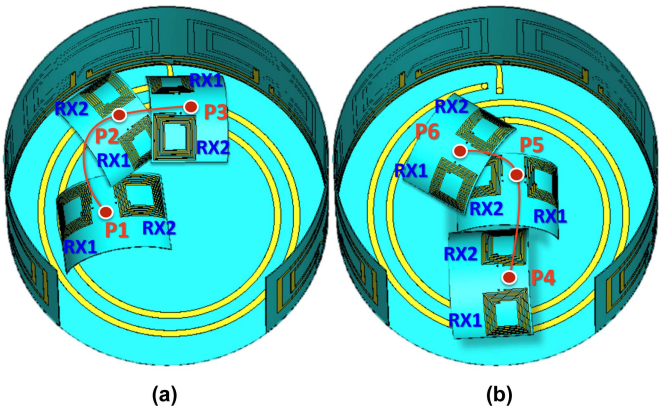

FIGURE 3. Simulated RX positions (Pi = 1, …,6) within the TX multi-coil array arrangement inside the semi-cylindrical experimental chamber: positions (a) from 1 to 3, and (b) from 4 to 6. [19].

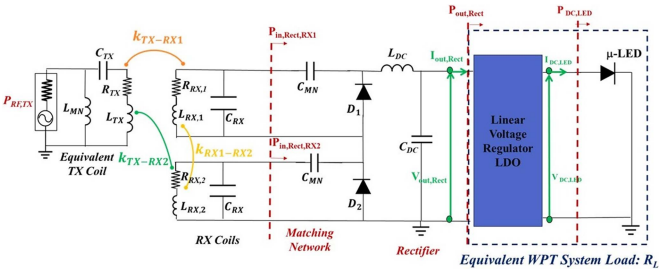

FIGURE 4. Equivalent circuit of the whole WPT link with focus on the RX subsystem: equivalent TX system, on the left, and detailed RX device including resonating coils, rectifiers, voltage regulator, and μ-LED, on the right. [19].

distributions were analyzed in terms of localized and averaged values, confirming that tissue absorption remains within conservative safety margins for the considered exposure conditions.

The complete system, including both TX and RX coils, was first tested by EM simulations considering six representative RX positions within the chamber, Pi (i = 1, …,6), depicted in Fig. 3, where each position also considers different cases of relative RX–TX relative coil displacement and angular orientation on the chamber lateral wall and floor, to emulate possible angular orientation scenarios of the mouse. The objective of this analysis was to optimize the power transfer efficiency (PTE) of the inductive link, ensuring reliable performance regardless of the mouse's movements during the in vivo experiment. Afterward, the EM-simulated impedance matrix of the resulting three-port circuit has been imported into the EM circuit simulator, where a non-linear EM/circuit co-design of the WPT has been carried out to fine-tune the overall WPT system, whose circuit-equivalent representation is shown in Fig. 4.

On the TX side, the series-connected multi-coil array is represented by an equivalent series inductance $L_{TX,eq}$ and resistance $R_{TX,eq}$, both extracted from EM simulations, and driven by a power generator ($P_{RF,TX}$ = 31.78 dBm, corresponding to approximately 1.5 W). On the RX side, the two identical receiving coils are modeled with inductances $L_{RX,i=\ 1,2}$, in series with their respective loss resistances $R_{RX,i=\ 1,2}$.

To enhance RF-to-RF PTE, a capacitor C_{TX} = 68 pF is series-connected to $L_{TX,eq}$ and two capacitors C_{RX} = 270 pF are connected in parallel to $L_{RX,i=\ 1,2}$, thus realizing a series-parallel resonant link at 13.56 MHz. In the proposed system, the TX coil was configured with a series resonance network. This topology minimizes the impedance at resonance, making it predominantly resistive and therefore well matched to the 50-Ω output impedance of the RF source. As a result, maximum power can be delivered from the generator to the TX coil. Conversely, the receiving coil employs a parallel resonance configuration, which increases the input impedance of the RX stage and provides a better match to the rectifier input impedance at the operating frequency and power conditions. This complementary matching strategy improves overall PTE and ensures stable system operation under varying load conditions.

At the resonant TX side, an additional inductance L_{MN} = 100 nH has been introduced to fine-tune the matching between the generator's internal 50-Ω resistance and the input impedance of the WPT link; similarly, each RX resonant coil is connected to a single-stage rectifier through a capacitance C_{MN} = 47 pF to improve the matching. The Skyworks RF Schottky diodes (SMS-3923, 46 V breakdown) have been used: the rectifier diodes are cascaded and connected to the DC output through a low-pass filter (comprising an inductor L_{DC} = 22 μH and a capacitor C_{DC} = 47 nF). Thus, a pure DC input to the Analog Devices LT1962 low-dropout (LDO) linear voltage regulator is ensured. The regulator is responsible for providing a stable output voltage $V_{DC,LED}$ = 2.8 V at the μ-LED input. For the present case, the 465-nm Cree TR2227 blue LED (270 x 220 x 50 μm^3) has been considered.

In the present design, the LDO-based regulation stage shown in Fig. 4 is adopted under the assumption of duty-cycled powering aligned with apnea-monitoring periods, rather than continuous operation. Physiological sensing (e.g., genioglossus electromyography (ggEMG) or blood oxygen saturation) is required only during sleep, when obstructive apnea events may occur; the external WPT link is therefore enabled only during these intervals. Under this scheme, the regulated 3 V output provided by the LDO regulator ensures stable supply to the μ-LED and potential low-power sensing electronics without requiring intermediate energy buffering.

An alternative approach involving a dedicated power-management integrated circuit and supercapacitor-based storage was evaluated but deemed unsuitable, as it would significantly increase implant size and mechanical complexity due to the need for additional matching networks, charge-management circuitry, and high-value capacitors. These constraints are incompatible with subdermal implantation in mice. Given the predictable activation windows and the measured worst-case harvested power, the compact LDO-based voltage regulator architecture provides a fully adequate power-management solution.

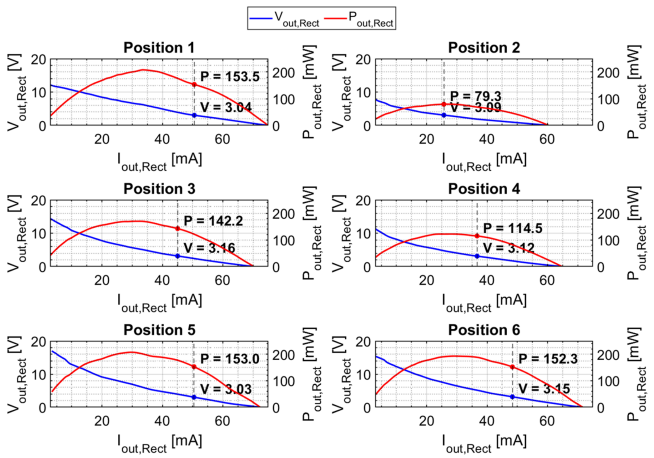

FIGURE 5. MPPT performance of the simulated circuit at each position Pi = 1,..,6; left y-axis: rectifier output voltage $V_{out,Rect}$, right y-axis: rectifier DC output power $P_{out,Rect}$. All graphs are plotted as a function of the rectifier output current $I_{out,Rect}$.

All these circuit values have been determined through the above-mentioned EM/circuit co-design using the nonlinear harmonic balance simulator. The LED's power consumption was defined to ensure a radiant power of at least 5 mW, which, based on physiological measurements, has been identified as the minimum intensity threshold required to successfully stimulate the hypoglossal nuclei and induce muscle contraction.

According to the datasheet, biasing the μ-LED at 2.8 V, a 5-mW light output can be achieved, consuming approximately 10 mW. Since the regulator can be configured to provide a stable output voltage of 3 V, a 40-Ω series resistance is introduced between the regulator and the μ-LED to control the forward current and ensure stable operation. The overall design and optimization process considered the regulator's constraints, as the rectifier output voltage must remain within the input voltage limits imposed by the regulator: to ensure a stable 3 V output, the regulator requires a minimum input voltage of 3.05 V, given its minimum dropout voltage of 50 mV. Therefore, the optimization has also been focused on ensuring that, regardless of the animal's position, the rectifier can provide an output voltage between 3.05 V and 20 V. Additionally, at the minimum output voltage of 3.05 V, the rectifier must supply enough current to meet the μ-LED's minimum power requirement of 10 mW. Fig. 5 shows the maximum power point tracking (MPPT) performance of the simulated circuit for the six reference positions of Fig. 3. The left axis represents the rectifier output voltage $V_{out,Rect}$, while the right axis shows the rectifier DC output power $P_{out,Rect}$, both plotted as a function of the rectifier output current $I_{out,Rect}$. It can be observed from these results that, for all simulated positions, the output DC power at the minimum rectifier voltage of 3.05 V is consistently well above the threshold required for successful optical stimulation. This ensures that, if a microcontroller unit (MCU) is inserted between the regulator and the μ-LED to generate pulsed stimulation, the rectifier would still be able to supply sufficient power to meet the combined consumption of both the MCU and the μ-LED. Moreover, these results also confirm that the rectifier output voltage never reaches the upper limit of 20 V, thus guaranteeing safe operation of the voltage regulator. In addition, at the maximum rectifier voltage, the corresponding input current to the regulator remains above the minimum required for proper regulation, further providing stable performance across all operating conditions.

III. WPT LINK EXPERIMENTAL CHARACTERIZATION

To achieve a conformal and flexible design, the system prototype was fabricated on a 25-μm-thick Kapton substrate ($\varepsilon_r = 3.4$, $tan(\delta) = 0.01$) with 35-μm-thick copper metallization (Fig. 1(b)). The inherent flexibility of Kapton allows the TX to conform seamlessly to the chamber's curved structure and the RX to fit comfortably to the mouse's back. The weight of the receiver prototype intended for subcutaneous implantation on the mouse's back was measured and found to be 600 mg. Considering an average mouse body weight of 22.5 g, the device corresponds to approximately 2.7% of the total body weight. This indicates that the implant is unlikely to affect the animal's natural movements, posture, or overall body load, thereby minimizing mechanical interference and implantation impact.

The following sections present the experimental validation of the proposed platform, including the characterization of the RF-to-RF link, the assessment of the overall WPT system performance, and in vivo testing on mice to evaluate the device's capability to wirelessly drive tongue muscle stimulation, thereby demonstrating the effectiveness of the fully wireless optogenetic system.

A. RF-TO-RF MEASURED EFFICIENCY ESTIMATION

The impedance values of the fabricated TX and RX prototypes in Fig. 1(b) were first extracted employing the Keysight N9952A FieldFox vector network analyzer (VNA), leading to the following values consistent with the simulated ones: $L_{TX,eq} = 1.92$ μH and $R_{TX,eq} = 1.5$ Ω for the TX and $L_{RX,i=1,2} = 0.44$ μH and $R_{RX,i=\ 1,2} = 0.76$ Ω for the RX coils. Given the measured impedances of the three coils, their quality factors were calculated as:

$$Q_{TX} = \omega \frac{L_{TX}}{R_{TX}}, \tag{1}$$

$$Q_{RX,i=1,2} = \omega \frac{L_{RX,i=1,2}}{R_{RX,i=1,2}}, \tag{2}$$

resulting in $Q_{TX} = 104$ and $Q_{RX,i=\ 1,2} = 53$, at $f = 13.56$ MHz and $\omega = 2\pi f$.

The RX coils were positioned at the six representative spatial locations shown in Fig. 3, covering different coupling scenarios. For each position, two distinct configurations (i.e., Setup 1 and Setup 2) were considered, as illustrated in Fig. 6: Setup 1 represents the awake mouse, with the RX coils placed in a saddle-like position on the back, while Setup 2 simulates a possible sleeping posture, with the RX coils rotated

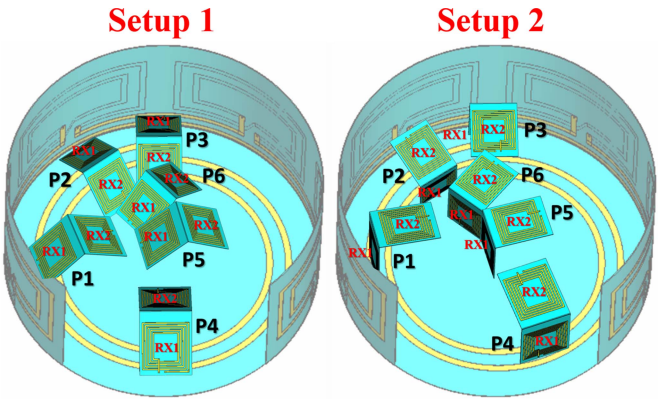

FIGURE 6. Measured RX positions (Pi = 1, …,6) and orientations, for Setup 1 and Setup 2, within the TX multi-coil array arrangement inside the semi-cylindrical experimental chamber [21].

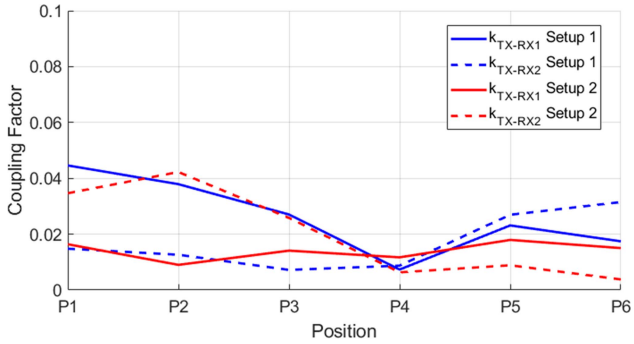

FIGURE 7. Coupling factors between TX and RX1 ($k_{TX\text{-}RX1}$), and between TX and RX2 ($k_{TX\text{-}RX2}$) placed in the six spatial positions Pi = 1,..,6 for Setup 1 and Setup 2.

by 45 degrees to emulate the mouse lying on its side. These setups were selected to reproduce the range of angular orientations and positions that the mouse may assume during in vivo experiments, allowing a comprehensive assessment of the system robustness. Notably, our system demonstrates improved stability compared to previous works in the literature [17] under similar real-world relative coil displacement and angular orientation scenarios, since the RX coils placed on the mouse's back experience a more limited range of motion than those positioned on the skull, reducing sensitivity to positional variations.

First, the coupling coefficients between the TX and one RX only are derived from measurements for the two setups of Fig. 6 and for the respective six locations: as expected, the results shown in Fig. 7 demonstrate that using a single RX leads to significant coupling degradation for certain mouse positions, thereby confirming the effectiveness and necessity of the dual-receiver configuration proposed in this work.

Indeed, the total effective coupling factor k_{TOT} must be considered for the present implementation, which can be calculated as follows [23]:

$$k_{TOT} = \frac{1}{\sqrt{2}} \frac{(k_{TX-RX1} + k_{TX-RX2})}{\sqrt{1 + k_{RX1-RX2}}}, \tag{3}$$

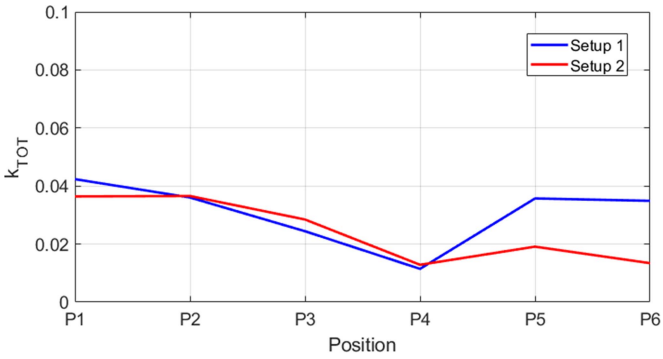

FIGURE 8. Total effective coupling factor k_{TOT} for the two-receivers setup; measurements with both setups and six different positions Pi (i = 1,..,6) have been evaluated.

which accounts for the overall link when multiple receivers are present and represents the effect of the combined coupling between the TX coil and each RX coil, as well as the coupling between the two RXs simultaneously [22]. The results derived by measurements are shown in Fig. 8 for the two setups, showing the advantage of the proposed combined two-RX solution. The coupling factor between RX1 and RX2 ($k_{RX1\text{-}RX2}$) has also been measured, and it results to be equal to 0.017. Indeed, as shown in Fig. 8, k_{TOT} is slightly lower than the superposition of the individual coupling factors, probably due to the small coupling between the two receivers.

Based on these measurements, the RF-to-RF efficiency of the inductive link was estimated for each receiver using the multiport network approximation [25], [26]. The efficiencies of the TX–RX1 link and the TX–RX2 link are given by (4) and (5), respectively, and shown at the bottom of the next page.

The efficiency values reported in this work were estimated using an analytical model derived for magnetically coupled resonant systems. The expression is valid under the assumption of resonant operation, where all coils are tuned to the same frequency, and weak to moderate coupling conditions, typically when the term $k^2{}_{TX\text{-}RX} \cdot Q_{TX} \cdot Q_{RX.} < 1$. In this regime, the energy transfer between coils can be accurately approximated by the product of the coupling coefficient and the quality factors of the resonators. Furthermore, the model assumes perfect impedance matching at both the TX and RX sides, so that no additional losses are introduced by mismatch or parasitic elements. Under these conditions, the simplified analytical formulation provides a reliable estimation of the RF-to-RF efficiency and allows meaningful comparison between different coil configurations and receiver placements.

As shown in Fig. 9, the estimated RF-to-RF efficiency exhibits clear dependence on the positioning of the receivers. While peak efficiencies approach 80–85% for the best spatial configurations, mutual loading effects reduce the efficiency in the less favorable cases (i.e., P4 for Setup 1 and P2 for Setup 2).

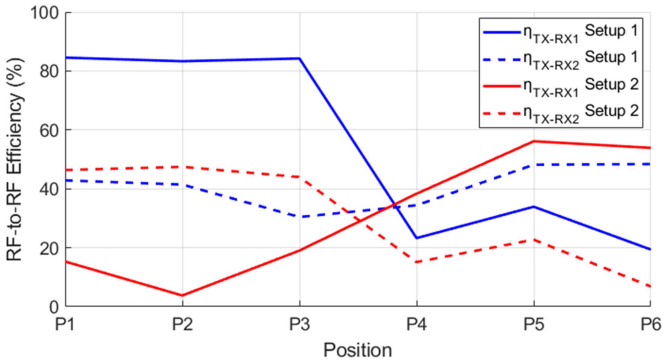

FIGURE 9. Estimated RF-to-RF efficiencies between TX and RX1 ($\eta_{TX\text{-}RX1}$), and between TX and RX2 ($\eta_{TX\text{-}RX2}$) placed in the six spatial positions Pi = 1,..,6 for Setup 1 and Setup 2.

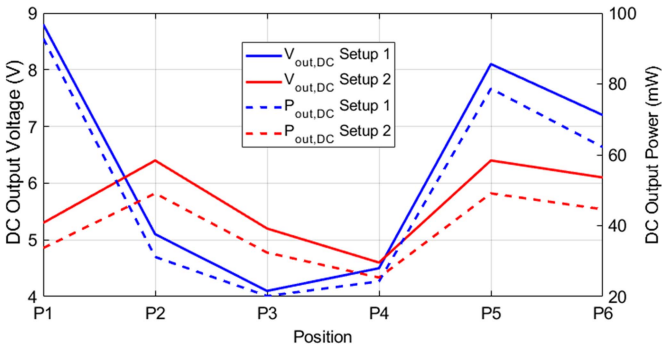

FIGURE 10. Measured rectifier output DC voltage ($V_{out,DC}$) and power ($P_{out,DC}$) at optimal load. The measurements have been performed in the six spatial positions Pi = 1,..,6 for Setup 1 and Setup 2.

B. RF-TO-DC EFFICIENCY MEASUREMENTS

To assess the practical overall performance of the system, RF-to-DC output measurements were performed at the rectifier output (described in Section II-B), with the optimal load selected for the RX system (834 Ω); in particular, the rectifier output voltage ($V_{out,DC}$) and output power ($P_{out,DC}$) have been evaluated across the six positions and for both setups with a power $P_{RF,TX} = 31.78$ dBm (approximately equal to 1.5 W) delivered from the RF generator (Keysight N5183B MXG X-Series Microwave Analog Signal Generator) to the TX device.

Fig. 10 reports the measured DC voltage and power at the rectifier output under optimal load conditions. As expected, these results are strongly correlated with the coupling factors measured earlier: the higher the coupling factors, the higher the DC output voltage and power.

Finally, Fig. 11 summarizes the overall RF-to-DC efficiency of the complete WPT system, from the RF power delivered to the transmitter to the DC power available at the

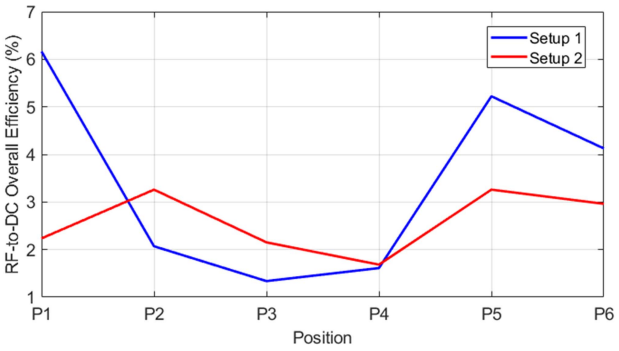

FIGURE 11. Measured overall $\eta_{RF,TX\text{-}DC}$ WPT system percentage efficiency considering (6).

rectifier output. The RF-to-DC efficiency is calculated as follows:

$$\eta_{RF,TX-DC} = \frac{P_{out,DC}}{P_{RF,TX}}. \tag{6}$$

Although the RF-to-RF efficiency of the inductive link can reach relatively high values, the measured end-to-end efficiency exceeds 6% for the best position (i.e., P1 for Setup 1). Nevertheless, these values are remarkable when considering the large size mismatch between the transmitting and receiving coils, which represents a particularly challenging condition for efficient WPT.

The experimental results show that RF-to-RF efficiency depends on spatial positioning and coil alignment, with peak efficiency at positions of highest coupling. However, despite alignment variations, the system maintains a robust link across the entire mouse plethysmograph surface. In multi-receiver configurations, power is delivered simultaneously to both receivers, increasing total transferred power compared to a single-receiver setup, demonstrating the link's reliability and suitability for multiple devices.

Considering the measured coupling factors, RF-to-RF efficiencies, and rectifier outputs, the end-to-end efficiency is consistently confirmed. Even at the most misaligned configuration (Setup 1, position P3), the delivered DC power reached 20 mW, well above the 10-mW required to drive the μ-LED and to achieve the minimum 5-mW optical output power for effective neurostimulation.

While the coupling coefficients and quality factors were experimentally obtained in air, direct measurements in live animals were not performed. This choice was motivated by the desire to prioritize functional validation of the full optogenetic platform and to avoid unnecessary invasiveness during

$$\eta_{RF-to-RF,\ TX-RX1} = \frac{\left(k^2_{TX-RX1} \cdot Q_{TX} \cdot Q_{RX1}\right)}{1 + k^2_{TX-RX1} \cdot Q_{TX} \cdot Q_{RX1} + k^2_{TX-RX2} \cdot Q_{TX} \cdot Q_{RX2} + k^2_{RX1-RX2} \cdot Q_{RX1} \cdot Q_{RX2}}. \tag{4}$$

$$\eta_{RF-to-RF,TX-RX2} = \frac{\left(k^2_{TX-RX2} \cdot Q_{TX} \cdot Q_{RX2}\right)}{1 + k^2_{TX-RX1} \cdot Q_{TX} \cdot Q_{RX1} + k^2_{TX-RX2} \cdot Q_{TX} \cdot Q_{RX2} + k^2_{RX1-RX2} \cdot Q_{RX1} \cdot Q_{RX2}} \tag{5}$$

preliminary feasibility studies. The robustness of the proposed system to postural and angular variations was instead systematically investigated through full-wave numerical simulations, as described in Section II, by analyzing multiple receiver orientations and spatial positions that emulate the most critical real-world translational and angular misalignment scenarios between the TX and RX coils. Future work will include systematic experimental characterization of tissue loading effects through in vivo measurements under different anatomical and postural conditions of the mouse.

IV. IN VIVO MEASUREMENTS OF OPTOGENETIC STIMULATION

A. ANIMALS AND VIRAL INJECTIONS

The in vivo tests of the wireless, battery-free device were performed on an adult male mouse (wild-type, C57BL/6J background) maintained at 23 °C under a 12:12 h light-dark cycle (lights on at 9 am, Zeitgeber Time 0, ZT0) with free access to food (4RF21 diet, Mucedola, Italy) and water. For system validation, a prototype device was implanted in an anesthetized mouse (20–25 g, skull 2 x 1 cm) to modulate tongue contractions via optogenetic stimulation of the hypoglossal nucleus. The mouse under study had been previously engineered, through the injection of a specific virus, in order to selectively express the photosensitive receptors in the hypoglossal nucleus (see Appendix for more details). A commercial LED was then inserted into the brain and programmed to deliver light pulses at 5 Hz and subsequently at 1 Hz while tongue contractions were continuously monitored, as described in detail in the following paragraph.

B. IN VIVO EXPERIMENTAL MEASUREMENT RESULTS FOR OPTOGENETIC STIMULATION AND TONGUE MUSCLE RECORDING

Under general anesthesia (2% isoflurane in O_2), the mouse was placed in the supine position, and a small midline incision was performed in the submental region. For the acute differential ggEMG signal detection, two multi-stranded perfluoroalkoxy (PFA)-coated stainless-steel wires were inserted in the targeted GG muscle from the base of the tongue using a 27G needle [27]. The ggEMG signal was amplified, filtered between 300 and 500 Hz using Model 1700 Differential AC Amplifier (A-M Systems, USA) and digitized at a sampling rate of 500 Hz.

Once a stable ggEMG signal was obtained, the mouse was positioned in the stereotaxic frame with the snout secured in an anesthetic mask. Before proceeding with the implantation of the optogenetic device, the radiant power at the tip of the 470 nm-blue commercial LED selected for these measurements (dimensions: 1 x 0.5 mm^2) was measured using a power meter (PM100D, Thorlabs, USA) connected to a photodiode power sensor (S120C, Thorlabs, USA), and it was able to deliver a measured radiant flux of 2.4 mW. The LED was then attached to the tip of a 25G needle, secured to the stereotaxic frame holder, and inserted into the brain at the midline (i.e., at a mediolateral coordinate of 0 mm), –7.20 mm posterior, and –4.7 mm dorsoventral to bregma just above the virus injection site [28]. The functional tongue muscle response was tested at two different stimulating frequencies. First, the LED was set to deliver light at 5 Hz (stimulating and interval pulse duration set at 100 ms) and then, at 1 Hz (stimulating and interval pulse duration set at 500 ms). Fig. 12 shows the in vivo experimental setup: the TX and RX devices are positioned to enable WPT, while the mouse is placed under general anesthesia in a stereotaxic frame to allow precise implantation of the LED device into the brain. This configuration ensures stable conditions for surgery and subsequent optogenetic stimulation experiments.

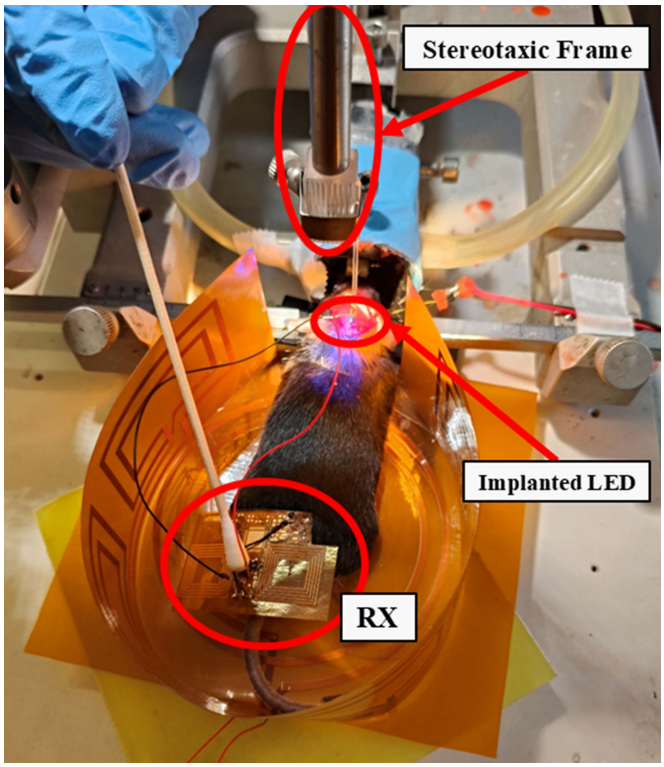

FIGURE 12. In vivo measurement setup with TX and RX devices and the mouse under general anesthesia in a stereotaxic frame for LED implantation in the brain.

Figs. 13–15 illustrate the natural tongue ggEMG activity and the corresponding responses to optogenetic light stimulation at two different frequencies (1 Hz and 5 Hz). The measurements were carried out over a total interval of 212 seconds. Within this window, periods with no stimulation (natural activity) and periods with stimulation at the two frequencies were analyzed and are represented in the following figures.

Fig. 13 reports a representative segment of ggEMG activity in the absence of light stimulation, showing the natural periodic tongue muscle signal (panel (b)) and its short-term integral (panel (c)), whereas Figs. 14 and 15 correspond to the trials with light stimulation at 1 Hz and 5 Hz, respectively. In these figures, panel (a) shows the square-wave light intensity (mW) applied to the tissue, panel (b) displays the normalized

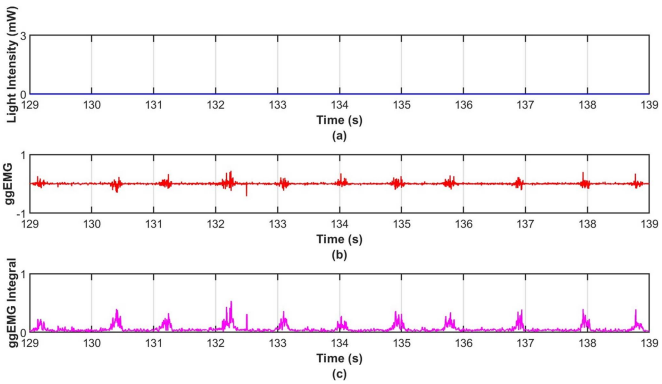

FIGURE 13. Tongue ggEMG activity in the absence of light stimulation: (a) Light intensity, (b) normalized ggEMG signal, and (c) short-term integral of the ggEMG signal.

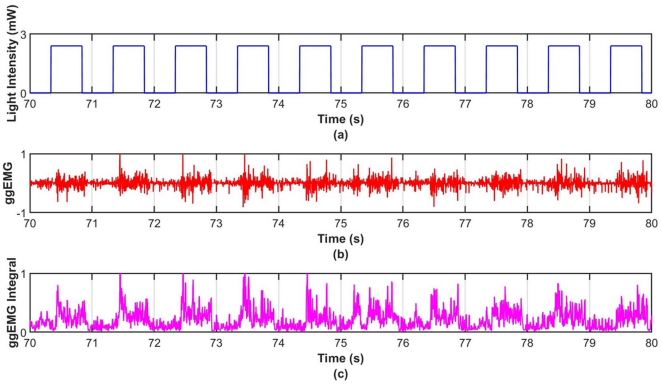

FIGURE 14. Light stimulation at 1 Hz and corresponding tongue ggEMG response: (a) Light intensity, (b) normalized ggEMG signal, (c) short-term ggEMG integral.

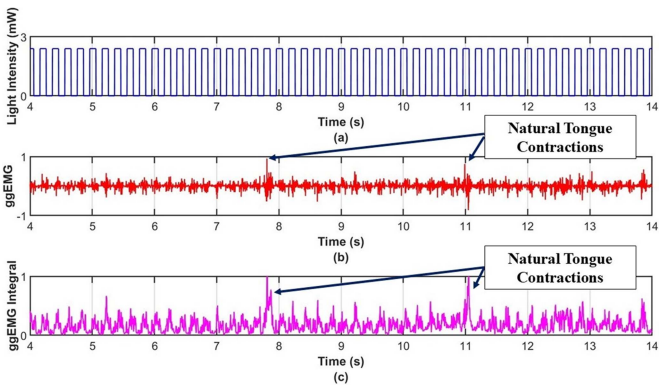

FIGURE 15. Light stimulation at 5 Hz and corresponding tongue ggEMG response: (a) Light intensity, (b) normalized ggEMG signal, and (c) short-term ggEMG integral. The superposition of a natural contraction and a light-induced response is also highlighted at 7.8 and 11 seconds.

ggEMG signal, and panel (c) presents the short-term integral of the ggEMG signal. The time axis represents the absolute time relative to the onset of stimulation, defined as time zero, which allows temporal alignment between the applied light stimulus and the physiological response.

The short-term ggEMG integral was computed as the cumulative sum of the absolute value of the ggEMG signal over a moving window of 0.01 seconds (corresponding to the 500 Hz sampling frequency). This representation highlights the instantaneous muscular activity and emphasizes the cumulative response to each light pulse. Both the ggEMG signal and its integral were normalized with respect to the maximum value obtained over the entire 212-second recording, to facilitate direct comparison across different conditions (including time intervals with and without light stimulation) and to emphasize relative changes in activity. Relative to this normalization, it can be observed that the amplitude of the responses to light stimulation is substantially higher than that of the natural, unstimulated tongue activity.

Moreover, in Fig. 15, it is also possible to notice that around 7.8 and 11 seconds, there is a superposition of a natural contraction and a light-induced response.

These representations provide a clear visualization of how tongue muscle activity is modulated by the frequency of light stimulation, and how the short-term integral captures the cumulative response within each brief window following each stimulus.

V. CONCLUSION

This work has presented a fully wireless and battery-free optogenetic platform for and the stimulation of hypoglossal motoneurons in small-sized murine models of obstructive sleep apnea, enabled by a conformal near-field WPT system operating at 13.56 MHz. The entire platform has been specifically developed for small rodents typically employed in preclinical studies, and the implant has been purposely miniaturized to meet the anatomical and experimental requirements of this type of model. The proposed design ensures robust energy transfer regardless of animal orientation or position, and in vivo experiments confirmed its capability to induce tongue muscle contractions with sufficient radiant power while maintaining limited invasiveness. These results demonstrate the feasibility of using lightweight, wireless, and battery-free optoelectronic implants to overcome the limitations of conventional fiber-based systems, enabling more naturalistic and reproducible behavioral studies.

In perspective, several directions for improvement remain open. The integration of optimized light-emitting devices, such as next-generation μ-LEDs, may further reduce implant dimensions, minimize power consumption, and enhance optical efficiency. In parallel, future studies will include dedicated in vivo experimental investigations of tissue-induced variations in mutual inductance and quality factor, in order to further refine the electromagnetic modeling of biological loading effects. In addition, the development of subdermal receiver modules will be pursued to increase biocompatibility, mechanical stability, and long-term reliability, thereby paving the way for chronic studies in freely moving animals. Together, these advancements would consolidate the proposed platform as a robust technological enabler for preclinical optogenetic research and provide a foundation toward future

translational applications in neuromodulation therapies for sleep-disordered breathing.

APPENDIX

A. ETHICAL APPROVAL

The study protocol complied with the EU Directive 2010/63/EU for animal experiments and was approved by the Committee on the Ethics of Animal Experiments of the Italian Ministry of Health (Prot. no. 34/2023_PR). The experiments were carried out according to the guidelines of the animal welfare committee of the University of Bologna, Italy, and ARRIVE guidelines. All efforts were made to minimize animal suffering.

B. VIRAL INJECTIONS

To achieve precise anatomical localization and expression of light-sensitive ChR2 employed an adeno-associated viral (AAV) vector carrying the plasmid hSyn-hChR2(H134R)-EYFP has been used. This viral vector ensured the selective expression of ChR2 in neurons (due to the presence of the hSyn promoter) and the possibility of fluorescence detection of transfected cells (due to the presence of the EYFP fluorescent gene report). The AAV was injected into the rostral portion of the hypoglossal nucleus (total volume: 400 nL, injection speed: 10 nL/s, titer: 1 x 10^{11} vg per ml) which contains motoneurons innervating intrinsic and extrinsic tongue muscles, including the GG muscle [29]. The mouse was anaesthetized (2% isoflurane in O_2) and placed in a stereotaxic frame (71000 Automated Stereotaxic Instrument, RWD Life Science Co., China). The skull was exposed, and a small burr hole was made to position a pre-pulled glass micropipette connected to a microsyringe injector pump. Stereotaxic coordinates relative to bregma were anteroposterior –7.20 mm, mediolateral 0.0 mm, dorsoventral –4.8 mm, based on [30]. After the injection, the mouse skin was sutured, and analgesic (Carprofen 0.1 mg, Pfizer, Italy) and antibiotic (Veterinary Rubrocillin, Intervet, Italy) were administered.

Five weeks later, the mouse underwent surgery to implant electrodes to record GG muscle activity and the optogenetic device into the rostral portion of the hypoglossal nucleus. This interval was necessary to achieve stable and high-level expression of ChR2 in the targeted motoneurons.

C. HISTOLOGY

After in vivo recordings, mice were processed for histological analyses. The mouse was terminally anaesthetized by overdose (4% isoflurane in 100% O_2), and perfused transcardially with 50 ml of ice-cold 0.1 M phosphate-buffered saline (PBS; pH 7.4) followed by 200 ml of paraformaldehyde solution (4% paraformaldehyde in PBS). The brain was removed and stored for 24 hours in the perfusion fixative at 4 °C, and cryoprotected in 20% sucrose in a PBS solution for 48 hours. 30 micrometers-thick serial coronal sections of the medulla were cut with a cryostat, mounted on glass slides and stained with 4′,6-diamidino-2-phenylindole (DAPI) to check the anatomical localization of ChR2 expression in hypoglossal motoneurons. Histological confirmation of viral targeting was achieved using the green fluorescent protein (GFP) filter (470/525 nm) of the fluorescent microscope (EVOS^{TM} M5000 Imaging System, cat. no. AMF5000SV, Thermofisher Scientific, USA) to detect enhanced yellow fluorescent protein (EYFP) expression (Fig. 16).

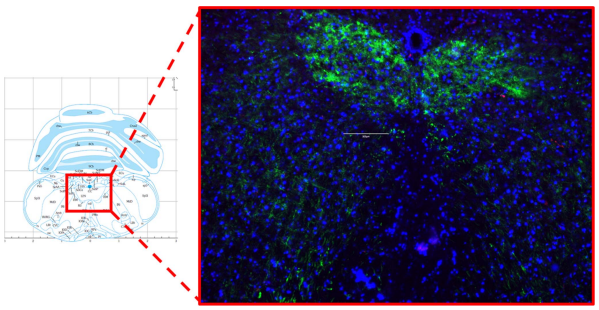

FIGURE 16. The right panel shows a histological image of the same area in a mouse injected with an AAV to selectively express light-sensitive receptors (ChR2) in the hypoglossal nucleus (12 N). Blue color is provided by DAPI solution which is useful for the anatomical localization of the area; green color represents the expression of the EYFP reporter gene which was concatenated with ChR2. Altogether, this image indicates the correct and selective expression of ChR2 in the 12 N. Scale bar: 300 μm.

ACKNOWLEDGMENT

This study was carried out also within the Spoke 13 of the MOST (Sustainable Mobility National Research Center).

REFERENCES

[1] L. Spicuzza, D. Caruso, and G. Di Maria, "Obstructive sleep apnoea syndrome and its management," *Therapeutic Adv. Chronic Dis.*, vol. 6, no. 5, pp. 273–285, 2015.
[2] X. Doyle et al., "Gene delivery to the hypoglossal motor system: Preclinical studies and translational potential," *Gene Ther.*, vol. 28, pp. 402–412, 2021.
[3] T. D. Bradley and J. S. Floras, "Obstructive sleep apnoea and its cardiovascular consequences," *Lancet*, vol. 373, no. 9657, pp. 82–93, 2009.
[4] J. S. Virk and B. Kotecha, "When continuous positive airway pressure (CPAP) fails," *J. Thoracic Dis.*, vol. 8, no. 10, pp. E1112–E1121, 2016.
[5] M. Arachchige and J. Steier, "Beyond usual care: A multidisciplinary approach towards the treatment of obstructive sleep apnoea," *Front. Cardiovasc. Med.*, vol. 8, 2022, Art. no. 747495.
[6] A. J. Kent, M. Lee, and J. R. Murphey, "Hypoglossal nerve stimulation therapy for the treatment of obstructive sleep apnea," *Neurotherapeutics*, vol. 18, no. 1, pp. 91–100, Jan. 2021.
[7] R. Costantino, G. Moffa, F. Rinaldi, A. Casale, and G. Fiorelli, "Hypoglossal nerve stimulation long-term clinical outcomes: A systematic review and meta-analysis," *Sleep Breath*, vol. 24, pp. 399–411, 2020.
[8] P. R. Eastwood et al., "Bilateral hypoglossal nerve stimulation for treatment of adult obstructive sleep apnoea," *Eur. Respir. J.*, vol. 55, no. 1, 2020, Art. no. 1901320.
[9] S. Jiang, X. Wu, N. Rommelfanger, Z. Ou, and G. Hong, "Shedding light on neurons: Optical approaches for neuromodulation," *Nat. Sci. Rev.*, vol. 9, 2022, Art. no. nwac007.
[10] S. Alvente, G. Matteoli, E. Miglioranza, G. Zoccoli, and S. Bastianini, "How to study sleep apneas in mouse models of human pathology," *J. Neurosci. Methods*, vol. 395, Jul. 2023, Art. no. 109923.
[11] A. M. Aravanis et al., "An optical neural interface: In vivo control of rodent motor cortex with integrated fiberoptic and optogenetic technology," *J. Neural Eng.*, vol. 4, no. 3, pp. S143–S156, 2007.
[12] P. Silva and L. Jacinto, "Wireless devices for optical brain stimulation: A review of current developments for optogenetic applications in freely moving mice," *Cell. Mol. Bioeng.*, vol. 18, no. 1, pp. 1–13, Nov. 2024.
[13] M. A. Rossi, V. Go, T. Murphy, Q. Fu, J. Morizio, and H. H. Yin, "A wirelessly controlled implantable LED system for deep brain optogenetic stimulation," *Front. Integrative Neurosci.*, vol. 9, 2015, Art. no. 8.

[14] A. Costanzo et al., "Electromagnetic energy harvesting and wireless power transmission: A unified approach," *Proc. IEEE*, vol. 102, no. 11, pp. 1692–1711, Nov. 2014.
[15] C. Y. Kim et al., "Soft subdermal implant capable of wireless battery charging and programmable controls for applications in optogenetics," *Nature Commun.*, vol. 12, no. 1, 2021, Art. no. 535.
[16] Y. Yang et al., "Wireless multilateral devices for optogenetic studies of individual and social behaviors," *Nature Neurosci.*, vol. 24, no. 7, pp. 1035–1045, 2021.
[17] G. Shin et al., "Flexible near-field wireless optoelectronics as subdermal implants for broad applications in optogenetics," *Neuron*, vol. 93, no. 3, pp. 509–521, 2017.
[18] J. Ausra et al., "Wireless, battery-free, subdermally implantable platforms for transcranial and long-range optogenetics in freely moving animals," *Proc. Nat. Acad. Sci.*, vol. 118, no. 30, 2021, Art. no. e2025775118.
[19] G. Battistini, E. Augello, G. Paolini, D. Masotti, and A. Costanzo, "Advancing obstructive sleep apnea therapy: A miniaturized wireless implant for battery-free optogenetic neurostimulation in mice," in *Proc. IEEE Wireless Power Technol. Conf. Expo*, 2025, pp. 1–4.
[20] E. Augello, G. Battistini, G. Paolini, S. Bastianini, G. Zoccoli, and A. Costanzo, "A conformal wireless power system for battery-free implantable optogenetic treatment of obstructive sleep apnea," in *Proc. IEEE MTT-S Int. Microw. Biomed. Conf.*, 2023, pp. 166–168.
[21] G. Battistini et al., "Soft, implantable, battery-free, and wirelessly controlled optoelectronic system for obstructive sleep apnea treatment," in *Proc. IEEE MTT-S Int. Microw. Biomed. Conf.*, 2024, pp. 87–89.
[22] A. Pacini, F. Benassi, D. Masotti, and A. Costanzo, "Design of a miniaturized omni-directional RF-to-DC IR-WPT," in *Proc. IEEE Wireless Power Transfer Conf.*, 2018, pp. 1–4.
[23] A. Pacini, F. Mastri, R. Trevisan, A. Costanzo, and D. Masotti, "Theoretical and experimental characterization of moving wireless power transfer systems," in *Proc. Eur. Conf. Antennas Propag.*, 2016, pp. 1–4.
[24] C. Baumgartner et al., "IT'IS database for thermal and electromagnetic parameters of biological tissues," Version 5.0, Aug. 21, 2025. [Online]. Available: https://itis.swiss/database
[25] A. P. Sample, D. T. Meyer, and J. R. Smith, "Analysis, experimental results, and range adaptation of magnetically coupled resonators for wireless power transfer," *IEEE Trans. Ind. Electron.*, vol. 58, no. 2, pp. 544–554, Feb. 2011.
[26] D. Ahn and S. Hong, "Effect of coupling between multiple transmitters or multiple receivers on wireless power transfer," *IEEE Trans. Ind. Electron.*, vol. 60, no. 7, pp. 2602–2613, Jul. 2013.
[27] O. Dergacheva, T. Fleury-Curado, V. Y. Polotsky, M. Kay, V. Jain, and D. Mendelowitz, "GABA and glycine neurons from the ventral medullary region inhibit hypoglossal motoneurons," *Sleep*, vol. 43, no. 6, Jun. 2020, Art. no. zsz301.
[28] J. A. Aggarwal, W.-Y. Liu, G. Montandon, H. Liu, S. W. Hughes, and R. L. Horner, "Measurement and state-dependent modulation of hypoglossal motor excitability and responsivity in vivo," *Sci. Rep.*, vol. 10, no. 1, Jan. 2020, Art. no. 550.
[29] R. de Sousa Costa, N. Ventura, T. de Andrade Lourenção Freddi, L. C. H. da Cruz, and D. G. Corrêa, "The hypoglossal nerve," *Seminar Ultrasound CT MR*, vol. 44, no. 2, pp. 104–114, Apr. 2023.
[30] G. Paxinos and K. B. J. Franklin, *Paxinos and Franklin's The Mouse Brain in Stereotaxic Coordinates*, 5th ed. Amsterdam, The Netherlands: Elsevier, 2019.

GIACOMO PAOLINI (Member, IEEE) received the M.Sc. degree in biomedical engineering and the Ph.D. degree in electronics, telecommunications, and information technologies engineering from the University of Bologna, Bologna, Italy, in 2016 and 2021, respectively. He was with the Interdepartmental Center for Industrial Information and Communication Technologies Research, University of Bologna, as a Research Fellow within the EU-supported Home Assistance Based on the Internet of Things for the AuTonomy of everybody project in 2016. He is currently a Junior Assistant Professor with the Department of Electrical, Electronic and Information Engineering "Guglielmo Marconi", University of Bologna. His research interests include microwave radar systems for biomedical applications, indoor positioning exploiting RFID technologies, near- and far-field wireless power transfer, and simultaneous wireless information and power transfer systems.

GIULIA BATTISTINI (Member, IEEE) received the M.Sc. (*cum laude*) degree in telecommunications engineering from the University of Bologna, Bologna, Italy, in 2022. She is currently working toward the Ph.D. degree in electronics, telecommunications, and information technologies engineering awaiting the final dissertation defense from the Department of Electrical, Electronic and Information Engineering "G. Marconi" University of Bologna. Her research focuses on wireless power transfer and energy harvesting for wearable and implantable biomedical devices, with emphasis on the design of miniaturized and conformal RF systems using low-cost and additive manufacturing technologies.

ELISA AUGELLO (Graduate Student Member, IEEE) received the M.Sc. degree in telecommunications engineering in 2022, where has been working toward the Ph.D. degree in electronics, telecommunications, and information technologies engineering with the University of Bologna, Bologna, Italy, since 2023. In 2022, she was with the Department of Electrical, Electronic and Information Engineering "G. Marconi," University of Bologna, as a Research Fellow within the framework of the project SONICA ("Optogenetic Stimulation of Hypoglossal Nuclei for Obstructive Sleep Apnea"). Her research interests include the application of artificial intelligence to computational electromagnetics, wireless power transfer for industrial and biomedical systems, and the design and optimization of implantable wireless devices.

STEFANO BASTIANINI received the M.Sc. degree in medical biotechnology and the Ph.D. degree in applied physiology and pathophysiology from the University of Bologna, Bologna, Italy, in 2007 and 2011, respectively. He is currently an Associate Professor of physiology with the Department of Biomedical and Neuromotor Sciences, University of Bologna. His research interests include many sleep disorders, such as sleep apnea and narcolepsy, and physiological regulations, such as cardiovascular, metabolic, and respiratory regulation in different mouse models of human pathology.

CHIARA BERTEOTTI received the M.Sc. degree in biological sciences and the Ph.D. degree in applied physiology and pathophysiology from the University of Bologna, Bologna, Italy, in 2003 and 2007, respectively. She is currently an Associate Professor of physiology with the Department of Biomedical and Neuromotor Sciences, University of Bologna. Her research interests include sleep disorders, such as narcolepsy and sleep apnea—and on cardiovascular, metabolic, and respiratory regulation studied through genetically modified mice and murine models of human diseases. She is also involved in studies investigating how early-life events shape body function, as well as in research on the bidirectional relationship between sleep and neurodegeneration.

DARIO CORACI received the M.Sc. degree in translational biomedical sciences – Neurobiology Track from the University of Parma, Parma, Italy, in 2024. He is currently working toward the Ph.D. degree with the Department of Biomedical and Neuromotor Sciences, University of Bologna, Bologna, Italy. His research interests include many sleep disorders, such as sleep apnea and narcolepsy, and physiological regulations, such as cardiovascular, metabolic, and respiratory regulation in different mouse models of human pathology.

VIVIANA LO MARTIRE received the degree in biological sciences and the Ph.D. degree in biomedical and neuromotor sciences in 2008 and 2012, respectively. Since 2004, she has been participating in the experimental activity of the PRISM LAB – Physiological Regulation in Sleeping Mice, aimed at studying the physiological regulation of blood pressure, body temperature, and breathing across the sleep–wake cycle in genetically modified mice and murine models of human diseases. She is currently an Associate Professor of physiology with the University of Bologna, Bologna, Italy.

DIEGO MASOTTI (Senior Member, IEEE) received the Ph.D. degree in electric engineering from the University of Bologna, Bologna, Italy, in 1997. In 1998, he was with the University of Bologna. From 2021, he has the role of coordinator of the Communications Engineering Master Degree course. He is currently a Full Professor of electromagnetic fields with the University of Bologna. His research interests include nonlinear microwave circuit simulation and design, with emphasis on nonlinear/electromagnetic co-design of integrated radiating subsystems/systems for wireless power transfer and energy harvesting applications. He has authored more than 90 scientific publications on peer reviewed international journals and more than 190 scientific publications on proceedings of international conferences. Dr. Masotti is a member of IEEE MTT-25 Wireless Energy Transfer and Conversion Technical Committee and the Editorial Board of Electronic Letters, of the Maximum Academic Press journal of Wireless Power Transfer, of IEEE ACCESS, IEEE JOURNAL OF RADIO FREQUENCY IDENTIFICATION, and member of the Paper Review Board of the main Journals of the microwave sector.

ELENA MIGLIORANZA received the M.Sc. degree in medical biotechnology from the University of Bologna, Bologna, Italy, in 2023. She is currently working toward the Ph.D. degree in applied physiology and pathophysiology with the Department of Biomedical and Neuromotor Sciences, University of Bologna. Her research interests include the pathophysiological mechanisms underlying sleep and sleep-related breathing disorders in genetically modified mouse models of human disease, the impact of perinatal stress on adult sleep–wake and respiratory phenotypes, and the bidirectional relationship between sleep and neurodegeneration.

SIMONE TROVARELLO (Member, IEEE) received the M.Sc. and Ph.D. degrees in electronics and telecommunications engineering from the University of Bologna, Bologna, Italy, in 2020 and 2025, respectively. He is currently a Postdoctoral Researcher with the Department of Electrical, Electronic, and Information Engineering "Guglielmo Marconi" with University of Bologna. His research interests include energy harvesting at microwave and mm-wave frequencies, ferroelectric materials for silicon-integrated reconfigurable applications, and noninvasive microwave sensors.

EMILIA VOLINO received the M.Sc. degree in health biology – forensic biology track from the University of Bologna, Bologna, Italy, in 2023. She is currently a Research Fellow with the Department of Biomedical and Neuromotor Sciences, University of Bologna. Her research interests include many sleep disorders, such as sleep apnea and narcolepsy, and physiological regulations, such as cardiovascular, metabolic, and respiratory regulation in different mouse models of human pathology.

GIOVANNA ZOCCOLI received the degree in medicine and surgery in 1987, a specialization in neurology in 1991, and the Ph.D. degree in experimental and clinical physiology, in 1995. Since 2003, she has been the Director of PRISM Lab in the Physiology section with the Department of Biomedical and Neuromotor Sciences, where physiological regulation is studied in genetically modified mice, models of human diseases. She is currently an Associate Professor of physiology with the University of Bologna, Bologna, Italy.

ALESSANDRA COSTANZO (Fellow, IEEE) has been a Full Professor with the University of Bologna, Bologna, Italy, since 2018. Prof. Costanzo holds three international patents and has authored more than 300 peer-reviewed papers in international conferences and journals. Her research interests include modern RF/microwave front-end design, including nonlinear device modeling, co-simulation, and co-design of active antenna systems and RF MIMO links. She focuses on developing innovative energy-autonomous wireless systems, including multi-band rectennas for wearable applications, ambient RF harvesting, and micro-power generation for IoT sensor nodes. Her work includes the design of wireless power transmission systems for various frequencies and power levels, utilizing both near-field and far-field techniques. She also explores solutions for energy-autonomous long-range UWB localization and simultaneous data and energy transfer. She co-founded the EU COST Action IC1301 WiPE; she is Past-Chair of the MTT-S TC-25, and Past VP for Publications of IEEE CRFID. She was the Chair of EuMC 2022 and IMBioC 2024. She is BoD Member of the Italian broadcasting company Rai Way S.p.A. and of the European Microwave Association. She is a fellow of IEEE, recognized for her contributions to nonlinear electromagnetic co-design in RF and microwave circuits.